

Dynamic susceptibilities of the single impurity Anderson model within an enhanced non-crossing approximation

Sebastian Schmitt,^{1,2} Torben Jabben,¹ and Norbert Grewe¹

¹*Institut für Festkörperphysik, Technische Universität Darmstadt, Hochschulstr. 6, D-64289 Darmstadt, Germany*

²*Lehrstuhl für Theoretische Physik II, Technische Universität Dortmund, Otto-Hahn Str. 4, D-44221 Dortmund, Germany*

(Dated: February 22, 2019)

The single impurity Anderson model (SIAM) is studied within an enhanced non-crossing approximation (ENCA). This method is extended to the calculation of susceptibilities and thoroughly tested, also in order to prepare applications as a building block for the calculation of susceptibilities and phase transitions in correlated lattice systems. A wide range of model parameters, such as impurity occupancy, temperature, local Coulomb repulsion and hybridization strength, are studied. Results for the spin and charge susceptibilities are presented. By comparing the static quantities to exact Bethe ansatz results, it is shown that the description of the magnetic excitations of the impurity within the ENCA is excellent, even in situations with large valence fluctuations or vanishing Coulomb repulsion. The description of the charge susceptibility is quite accurate in situations where the singly occupied ionic configuration is the unperturbed ground state; however, it seems to overestimate charge fluctuations in the asymmetric model at too low temperatures. The dynamic spin excitation spectra is dominated by the Kondo-screening of the impurity spin through the conduction band, i.e. the formation of the local Kondo-singlet. A finite local Coulomb interaction U leads to a drastic reduction of the charge response via processes involving the doubly occupied impurity state. In the asymmetric model, the charge susceptibility is enhanced for excitation energies smaller than the Kondo scale T_K due to the influence of valence fluctuations.

I. INTRODUCTION

The single impurity Anderson model (SIAM) describes an impurity of localized f -states with local Coulomb interaction embedded into a metallic host of non-interacting c -band electrons¹. In its simplest version it discards the possibility of a complex orbital structure of the impurity and models the local f -states through two-fold degenerate s -orbital. The Hamiltonian for the impurity reads

$$\hat{H}_f = \sum_{\sigma} \left(\epsilon^f \hat{f}_{\sigma}^{\dagger} \hat{f}_{\sigma} + \frac{U}{2} \hat{n}_{\sigma}^f \hat{n}_{\sigma}^f \right) \quad , \quad (1)$$

with $\hat{f}_{\sigma}^{\dagger}$ (\hat{f}_{σ}) and $\hat{n}_{\sigma}^f = \hat{f}_{\sigma}^{\dagger} \hat{f}_{\sigma}$ the usual creation (annihilation) and number operators for f -electron with spin σ , respectively. The local one-particle energy is given by ϵ^f , and the local Coulomb interaction is the usual density-density interaction proportional to the matrix element U . The non-interacting band states are modeled by a single band of Bloch states with crystal momentum \underline{k} characterized by the dispersion relation $\epsilon_{\underline{k}}^c$,

$$\hat{H}_c = \sum_{\underline{k}, \sigma} \epsilon_{\underline{k}}^c \hat{c}_{\underline{k}\sigma}^{\dagger} \hat{c}_{\underline{k}\sigma} \quad . \quad (2)$$

These two parts mix via a hybridization amplitude $V_{\underline{k}}$,

$$\hat{V} = \frac{1}{\sqrt{N_0}} \sum_{\underline{k}} \left(V_{\underline{k}} \hat{f}_{\sigma}^{\dagger} \hat{c}_{\underline{k}\sigma} + h.c. \right) \quad . \quad (3)$$

The total Hamiltonian is then the sum of these three terms

$$\hat{H} = \hat{H}_c + \hat{H}_f + \hat{V} \quad . \quad (4)$$

Even though the thermodynamics of the model can be solved exactly within the Bethe ansatz method^{2,3,4,5}, dynamic quantities can in general not be obtained exactly and one has to rely on approximations. The SIAM has been extensively studied with various methods, including the numerical renormalization group (NRG)^{6,7,8,9}, the (dynamic) density-matrix renormalization group ((D-)DMRG)^{10,11,12,13}, quantum Monte Carlo (QMC) methods^{14,15,16} and direct perturbation theory with respect to the hybridization^{17,18,19,20}. Especially with the development of the dynamical mean-field theory (DMFT)²¹, where the solution of an effective SIAM represents the essential step towards the solution of the correlated lattice system, the interest in accurate and manageable impurity solvers has increased. In particular, the calculation of lattice susceptibilities within DMFT^{22,23,24} needs a reliable strategy for susceptibilities of an effective impurity.

In this work, we extend the well established enhanced non-crossing approximation (ENCA)^{25,26} to the calculation of the static and dynamic susceptibilities of the impurity. Like many other approximations formulated within the direct perturbation theory with respect to the hybridization^{26,27,28,29,30,31}, the ENCA is thermodynamically conserving in the sense of Kadanoff and Baym^{32,33}. It extends the usual non-crossing approximation (NCA) to finite values of the Coulomb repulsion U via the incorporation of the lowest order vertex corrections, which are necessary to produce the right Schrieffer-Wolff exchange coupling and the order of magnitude of the low energy Kondo scale of the problem. As it will be shown in this work, the skeleton diagrams selected within the ENCA suffer from an imbalance between charge and spin exci-

tations. It can be stated quite generally, that the ENCA overestimates the influence of charge fluctuations. From the simpler NCA it is well known that some pathological structure appears near the Fermi level effectively increasing the ASR at temperatures below a pathology scale^{34,35} $T_{path} \approx 10^{-1} - 10^{-2} T_K$. Apart from some remaining pathological structure the ENCA has no further limitations. We will connect this in the following with an imbalance regarding the role of charge fluctuations included in the ENCA.

Compared to the “numerically exact” schemes like the renormalization group methods (RG), exact diagonalization (ED) or QMC, the direct perturbation theory has its advantages: (i) The approximations are free of systematic errors stemming from the discretization of the conduction band (RG and ED) or imaginary time (QMC). The continuum of band states is kept throughout the calculation, and dynamic Green functions are formulated with continuous energy variables. Thus, there are no discretization-artefacts³⁶ and there is no need for artificial broadening parameters^{37,38} or z -averaging^{39,40}. (ii) The coupled integral equations for dynamic quantities, which have to be solved numerically, are formulated on the real frequency axis, which renders the non-trivial numerical analytic continuation of a finite set of Fourier coefficients⁴¹ or deconvolution⁴² unnecessary.

II. THE ENHANCED NON-CROSSING APPROXIMATION SCHEME AND DYNAMIC SUSCEPTIBILITIES

In direct perturbation theory with respect to the hybridization term \hat{V} the “unperturbed” system is represented by the uncoupled ($V_{\underline{k}} = 0$) interacting impurity. This is diagonalized by the ionic many-body states $|M\rangle$

$$\hat{H}_f = \sum_M E_M \hat{X}_{M,M} \quad , \quad (5)$$

where the operators $\hat{X}_{M,M} = |M\rangle\langle M|$ are projectors on the eigenstates $|M\rangle$ and are diagonal versions of the so-called ionic transfer (or Hubbard) operators $\hat{X}_{M,M'} = |M\rangle\langle M'|$. For a simple s -shell the quantum numbers M characterize the empty $|0\rangle$, singly occupied with spin σ $|\sigma\rangle$ and doubly occupied $|2\rangle$ impurity states with the corresponding unperturbed eigenvalues $E_0 = 0$, $E_\sigma = \epsilon^f$ and $E_2 = 2\epsilon^f + U$, respectively. Furthermore, the partition function and dynamic Green function are expressed in terms of a contour-integration in the complex plane,

$$Z = Tr e^{-\beta \hat{H}} = \oint_C \frac{dz}{2\pi i} e^{-\beta z} Tr [z - \hat{H}]^{-1} \quad (6)$$

$$G_{A,B}(i\eta) = \frac{1}{Z} \oint_C \frac{dz}{2\pi i} e^{-\beta z} Tr \left\{ [z - \hat{H}]^{-1} \hat{A} \cdot [z + i\eta - \hat{H}]^{-1} \hat{B} \right\} \quad , \quad (7)$$

with $i\eta$ either a fermionic or bosonic Matsubara frequency depending on the type of the operators \hat{A} and \hat{B} . The contour \mathcal{C} encircles all singularities of the integrand, which are situated on the $\text{Im } z = 0$ and $\text{Im}(z + i\eta) = 0$ axes in a mathematical positive sense. Performing the trace over the c -electrons first, the reduced f -partition function Z_f , the f -electron one-body Green function $F_\sigma \equiv G_{f_\sigma, f_\sigma^\dagger}$ and generalized susceptibility $\chi_{M,M'} \equiv G_{\hat{X}_{M,M}, \hat{X}_{M',M'}}$ can be expressed as

$$Z_f = \sum_M \oint_C \frac{dz}{2\pi i} e^{-\beta z} P_M(z) \quad , \quad (8)$$

$$F_\sigma(i\omega_n) = \frac{1}{Z_f} \oint_C \frac{dz}{2\pi i} e^{-\beta z} \left[P_0(z) P_\sigma(z + i\omega_n) \Lambda_{0,\sigma}(z, i\omega_n) + P_{\bar{\sigma}}(z) P_2(z + i\omega_n) \Lambda_{2,\bar{\sigma}}(z + i\omega_n, i\omega_n) \right] \quad , \quad (9)$$

$$\begin{aligned} \chi_{M,M'}(i\nu_n) &= -\frac{1}{Z_f} \oint_C \frac{dz}{2\pi i} e^{-\beta z} \chi_{M,M'}(z, z + i\nu_n) \\ &= -\frac{1}{Z_f} \oint_C \frac{dz}{2\pi i} e^{-\beta z} \Gamma_{M,M'}(z, z + i\nu_n) \cdot \\ &\quad \cdot \Pi_{M'}(z, z + i\nu_n) \quad . \quad (10) \end{aligned}$$

Here $\Pi_M(z, z') = P_M(z)P_M(z')$ and the ionic propagators

$$P_M(z) = \langle M | \langle [z - \hat{H} + \hat{H}_c]^{-1} | c | M \rangle \quad (11)$$

$$\equiv \frac{1}{z - E_M - \Sigma_M(z)} \quad , \quad (12)$$

which describe the dynamics of an ionic state $|M\rangle$ are introduced. In equation (12) the ionic propagator is expressed with the help of the ionic self-energy $\Sigma_M(z)$. $\langle \dots \rangle_c = \frac{1}{Z_c} Tr_c (e^{-\beta \hat{H}_c} \dots)$ indicates that the trace is to be taken over the c -states only, and Z_c represents the partition function of the isolated c -system. In equations (9) and (10), $\Lambda_{M,M'}$ and $\Gamma_{M,M'}$ represent vertex functions to be specified later. These equations are graphically represented in Figure 1.

After re-writing the Hamiltonian in terms of the ionic transfer operators $\hat{X}_{M,M'}$, the resolvent operator is expanded with respect to \hat{V} , $[z - \hat{H}]^{-1} = [z - \hat{H}_f - \hat{H}_c]^{-1} \sum_{n=0}^{\infty} [\hat{V} [z - \hat{H}_f - \hat{H}_c]^{-1}]^n$. Consequently inserting the identity $\hat{1} = \sum_{c;M} |M\rangle\langle c|c\rangle\langle M|$ and using the representation (11) for the ionic propagators, this perturbation theory can be formulated with time-ordered Goldstone diagrams, representing the dynamics of the ionic states $|M\rangle$ and their hybridization processes⁶⁷. Approximations are then introduced for the self-energies Σ_M and vertex functions $\Lambda_{M,M'}$ and $\Gamma_{M,M'}$. In order to be able to describe non-perturbative many-body phenomena like the Kondo effect, certain classes of diagrams

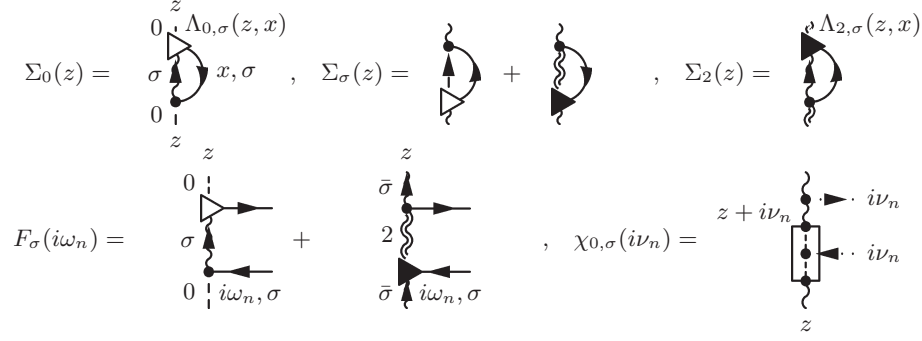


FIG. 1: Diagrammatic equations for the ionic self-energies (upper), f -electron Green function (lower left) and dynamic susceptibility (lower right, $\chi_{0,\sigma}(i\nu)$ as an example). The dashed, wiggly and double-wiggly lines represent the empty, singly occupied ($\bar{\sigma}$ represents the opposite of the spin σ) and doubly occupied ionic propagators, respectively. The triangles and boxes represent the appropriate vertex functions. The closed full lines in the upper graphs represent uncorrelated propagations in the c -band.

have to be re-summed up to infinite order, resulting in a formulation in terms of skeleton diagrams, and corresponding coupled integral equations for the relevant dynamic functions. Deriving these equations consistently through functional derivatives from one Luttinger-Ward functional Φ renders these approximations thermodynamically consistent.

Within the ENCA, the ionic self-energies and propagators have to be determined from the well known set of coupled integral equations^{25,26,43},

$$\begin{aligned} \Sigma_0(z) &= \sum_{\sigma} \int dx \Delta^+(x) P_{\sigma}(z+x) \Lambda_{0,\sigma}(z, x) \quad (13) \\ \Sigma_{\sigma}(z) &= \int dx \Delta^-(x) P_{\bar{\sigma}}(z-x) \Lambda_{0,\sigma}(z-x, x) \\ &\quad + \int dx \Delta^+(x) P_2(z+x) \Lambda_{2,\sigma}(z+x, x) \\ \Sigma_2(z) &= \sum_{\sigma} \int dx \Delta^-(x) P_{\sigma}(z-x) \Lambda_{2,\sigma}(z, x) \quad , \end{aligned}$$

where the vertex functions are given by

$$\Lambda_{0,\sigma}(z, z') = 1 + \int dx \Delta^+(x) P_{\bar{\sigma}}(z+x) P_2(z+z'+x) \quad (14)$$

$$\Lambda_{2,\sigma}(z, z') = 1 + \int dx \Delta^-(x) P_{\bar{\sigma}}(z-x) P_0(z-z'-x) \quad ,$$

and $\Delta^{\pm}(x) = \Delta(x)f(\pm x)$. The hybridization function $\Delta(x)$ is constructed from the c -band electrons

$$\Delta(x) = \frac{1}{N_0} \sum_{\mathbf{k}} |V_{\mathbf{k}}|^2 \delta(x - \epsilon_{\mathbf{k}}^c) \quad , \quad (15)$$

and $f(x) = 1/(e^{\beta x} + 1)$ is the Fermi function with $\beta = 1/T$ the inverse the temperature (note $\hbar = c = k_B = 1$). An additional set of integral equations has to be set up for the generalized susceptibilities $\chi_{M,M'}(z, z')$, which is shown graphically in Figure 2. In principle, there are 16 such functions, but for each quantum number M only the four functions $\chi_{M,0}(z, z')$, $\chi_{M,\sigma}(z, z')$, and $\chi_{M,2}(z, z')$ are

coupled. Due to the conserving nature of the ENCA, these equations are closely related to the ENCA expressions for the ionic self-energies; only some additional bosonic lines entering and leaving the site have to be introduced. Whereas the lowest order vertex corrections of equation (14) together with the ionic propagators (11) and self-energies (12), are sufficient to furnish a conserving approximation, the vertices $\Gamma_{M,M'}(z, z')$ for the susceptibilities (10) have to be iterated up to infinite order! The transcription of these graphs into formulas is straight forward but lengthy and will be omitted here.

In the case of infinitely large Coulomb repulsion $U \rightarrow \infty$, the ENCA reduces to the usual NCA, and all equations presented above approach the ones already known from the literature^{27,44}. In this sense, the ENCA is still referred to as non-crossing even though crossing diagrams are included. For approximations involving ‘‘real’’ crossing diagrams see^{26,29,30,45}.

The functions $\chi_{M,M'}(z, z')$ fulfill the symmetry relations

$$\chi_{M,M'}(z^*, z'^*) = \chi_{M,M'}(z, z')^* \quad (16)$$

and

$$\chi_{M,M'}(z, z') = \chi_{M,M'}(z', z) \quad , \quad (17)$$

which are revealed by inspection of the perturbation expansion. The susceptibilities also obey the sum rules

$$\sum_{M'} \chi_{M',M}(i\nu_n) = \langle \hat{X}_{MM} \rangle \delta_{i\nu_n,0} \quad (18)$$

$$\sum_M \chi_{M',M}(i\nu_n) = \langle \hat{X}_{M'M'} \rangle \delta_{i\nu_n,0} \quad (19)$$

$$\sum_{M,M'} \chi_{M',M}(i\nu_n) = \sum_M \langle \hat{X}_{MM} \rangle \delta_{i\nu_n,0} = \delta_{i\nu_n,0} \quad , \quad (20)$$

which arise from the completeness relation of the local ionic states, $1_f = \sum_M |M\rangle\langle M|$. These sum rules transform into equivalent statements for the functions $\chi_{M',M}(z, z')$,

$$\sum_{M'} \chi_{M',M}(z, z') = -\frac{P_M(z) - P_M(z')}{z - z'} \quad . \quad (21)$$

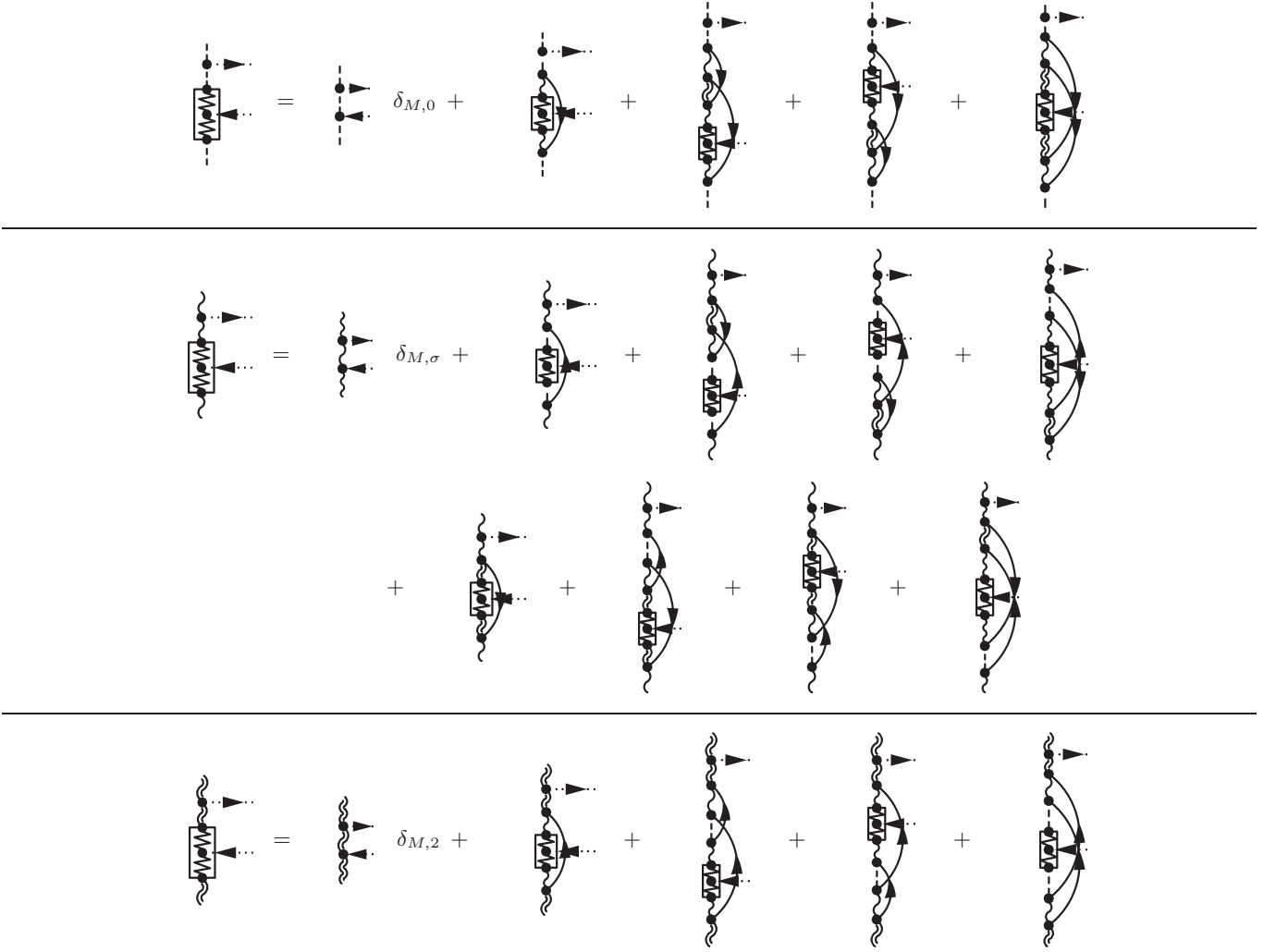


FIG. 2: System of integral equations for $\chi_{M,0}(z, z')$, $\chi_{M,\sigma}(z, z')$, and $\chi_{M,2}(z, z')$ within the ENCA. Zig-zag lines in the vertex part represent the ionic state M , which can either be empty, singly occupied or doubly occupied. The arrows entering and leaving each diagram carry the external bosonic frequency $i\nu$.

It can be analytically checked that the ENCA respects these sum rules. The form of equation (21) explicitly reveals the conserving nature of this approximation, since the sum of sets of two-particle correlation functions is determined by the corresponding one-particle correlation function, i.e. the ionic propagator. Insofar the equations (21) resemble generalized Ward-Identities.

In order to obtain the physical susceptibility as a function of a real frequency, the contour integration of equation (10) has to be performed, then the external bosonic Matsubara frequency can be analytically continued to the real axis, $i\nu_n \rightarrow \nu \pm i\delta \equiv \nu^\pm$ ($\delta > 0$ infinitesimal). The result of this procedure reads

$$\chi_{M,M'}(\nu^+) = \int_{-\infty}^{\infty} \frac{d\omega}{2\pi i} \left[Y_{M,M'}(\omega, \omega + \nu) - Y_{M,M'}(\omega, \omega - \nu)^* \right], \quad (22)$$

where the symmetry relations (16) were used and the defect quantities

$$Y_{M,M'}(x, y) = \frac{e^{-\beta x}}{Z_f} \left[\chi_{M,M'}(x^+, y^+) - \chi_{M,M'}(x^-, y^+) \right] \quad (23)$$

were defined. Due to the appearance of the exponential factor, a direct numerical evaluation of the defect quantities given the $\chi_{M,M'}$ is not possible and additional sets of integral equations have to be solved for the $Y_{MM'}$ (cf.^{46,47}).

In the following, only spin-symmetric situations are considered, and the propagators for opposite spins are identified, i.e. $P_\sigma = P_{\bar{\sigma}} \equiv P_\uparrow$, $\chi_{\sigma,\sigma} = \chi_{\bar{\sigma},\bar{\sigma}} \equiv \chi_{\uparrow,\uparrow}$, $\chi_{\bar{\sigma},\sigma} = \chi_{\sigma,\bar{\sigma}} \equiv \chi_{\uparrow,\downarrow} \dots$

A. Magnetic susceptibility

The relevant quantity for the magnetic susceptibility is the auto-correlation function of the z -component of the spin operator $\hat{S}^z \sim \hat{n}_\uparrow - \hat{n}_\downarrow = \hat{X}_{\uparrow,\uparrow} - \hat{X}_{\downarrow,\downarrow}$. This translates into the linear combination

$$\chi_{mag}(z, z') = \chi_{\uparrow,\uparrow}(z, z') - \chi_{\uparrow,\downarrow}(z, z') \quad , \quad (24)$$

which needs to be determined. Setting up the equations for this linear combination using the general equations depicted in Figure 2 leads to the cancellation of all spin-symmetric terms²⁴. The function $\chi_{mag}(z, z')$, decouples from the $\chi_{0,M}(z, z')$ and $\chi_{2,M}(z, z')$ and only one integral equation is obtained,

$$\begin{aligned} \chi_{mag}(z, z') = & \Pi_\uparrow(z, z') \left\{ \right. \\ & 1 - \int dx dy \Delta^+(x) \Delta^-(y) \left[P_2(z'+x) P_0(z-y) \right. \\ & \left. \left. + P_0(z'-y) P_2(z+x) \right] \chi_{mag}(z+x-y, z'+x-y) \right\} . \end{aligned} \quad (25)$$

The derivation of the corresponding defect equation for Y_{mag} along the lines of the definition (23) is straight forward, but will be omitted here for brevity.

B. Charge susceptibility

For the charge susceptibility the relevant quantity is the auto-correlation function of the charge operator $\hat{n} = \hat{n}_\uparrow + \hat{n}_\downarrow = \hat{X}_{\uparrow,\uparrow} + \hat{X}_{\downarrow,\downarrow} + 2\hat{X}_{2,2}$ leading to the dynamic function

$$\begin{aligned} \chi_{charge}(z, z') = & \chi_{\uparrow,\uparrow}(z, z') + \chi_{\uparrow,\downarrow}(z, z') \\ & + 2 \left(\chi_{2,2}(z, z') + \chi_{2,\uparrow}(z, z') + \chi_{\uparrow,2}(z, z') \right) \\ = & \chi_{2,2}(z, z') - \chi_{0,2}(z, z') + \chi_{0,0}(z, z') - \chi_{2,0}(z, z') \\ & + S_{0,\uparrow,2}(z, z') \quad . \end{aligned} \quad (26)$$

In the second equality sum rules like (21) were used. The function $S_{0,\uparrow,2}(z, z')$ is not relevant for dynamic susceptibilities, since it only contributes in the case of a vanishing external frequency $i\nu_n = 0$. The hole susceptibility, i.e. the auto-correlation function of the hole operator $\hat{h} = 2 - \hat{n} = 2\hat{X}_{0,0} + \hat{X}_{\uparrow,\uparrow} + \hat{X}_{\downarrow,\downarrow}$, is given by the same expression, only with a different contribution from the sum rules. Both of these contributions do not change the dynamic susceptibility since they produce only the necessary constant shift between the static ($i\nu_n = 0$) charge and hole susceptibility after the contour integration,

$$\chi_{hole}(i\nu_n) = \chi_{charge}(i\nu_n) + 4(1 - \langle \hat{n} \rangle) \delta_{i\nu_n, 0} \quad . \quad (27)$$

The dynamical quantities of interest are best obtained by setting up the integral equations for the linear combinations $c_{0,0} = \chi_{0,0} - \chi_{2,0}$, $c_{0,\uparrow} = \chi_{0,\uparrow} - \chi_{2,\uparrow}$ and

$c_{0,2} = \chi_{0,2} - \chi_{2,2}$, which read

$$\begin{aligned} c_{0,0}(z, z') = & \Pi_0(z, z') \left\{ 1 \right. \\ & + 2 \int dx \Delta^+(x) \left[\Lambda_{0,\uparrow}(z', x) + \Lambda_{0,\uparrow}(z, x) - 1 \right] c_{0,\uparrow}(z+x, z'+x) \\ & + 2 \int dx dy \Delta^+(x) \Delta^+(y) P_\uparrow(z'+x) P_\uparrow(z+y) \times \\ & \left. \left. \times c_{0,2}(z+x+y, z'+x+y) \right\} \right. \\ c_{0,\uparrow}(z, z') = & \Pi_\uparrow(z, z') \left\{ \right. \\ & \int dx \Delta^-(x) \left[\Lambda_{0,\uparrow}(z'-x, x) \right. \\ & \left. \left. + \Lambda_{0,\uparrow}(z-x, x) - 1 \right] c_{0,0}(z-x, z'-x) \right. \\ & + \int dx \Delta^+(x) \left[\Lambda_{2,\uparrow}(z'+x, x) \right. \\ & \left. \left. + \Lambda_{2,\uparrow}(z+x, x) - 1 \right] c_{0,2}(z+x, z'+x) \right. \\ & + \int dx dy \Delta^+(x) \Delta^-(y) \left[P_2(z'+x) P_0(z-y) \right. \\ & \left. \left. + P_0(z'-y) P_2(z+x) \right] c_{0,\uparrow}(z+x-y, z'+x-y) \right\} \end{aligned} \quad (28)$$

$$\begin{aligned} c_{0,2}(z, z') = & \Pi_2(z, z') \left\{ -1 \right. \\ & + 2 \int dx \Delta^-(x) \left[\Lambda_{2,\uparrow}(z', x) + \Lambda_{2,\uparrow}(z, x) - 1 \right] c_{0,\uparrow}(z-x, z'-x) \\ & + 2 \int dx dy \Delta^-(x) \Delta^-(y) P_\uparrow(z'-x) P_\uparrow(z-y) \times \\ & \left. \left. \times c_{0,0}(z-x-y, z'-x-y) \right\} . \end{aligned} \quad (30)$$

As can be seen, now all three linear combinations are coupled, which makes the numerical simulation of the full system inevitable. The corresponding defect equations are again determined in a straight-forward way, but are omitted here due to their length. Unfortunately, the system for the defect quantities becomes singular for vanishing external frequency $\nu \rightarrow 0$. This can be guessed, since the sum rule (21) translates into $\sum_{M'} Y_{M',M}(\omega, \omega + \nu) = -2\pi i \xi_M(\omega) / (\nu + i\delta)$ and implies, that the $Y_{M,M'}$ become of the order of $\frac{1}{\nu}$ for small ν , while on the other hand all terms in the integral equations stay at the order one. This becomes of some importance, when extracting static susceptibilities from calculations of the dynamic susceptibilities, where a very small but finite frequency is used. The resulting convergence problems are probably connected to the ones already mentioned in other studies⁴⁸.

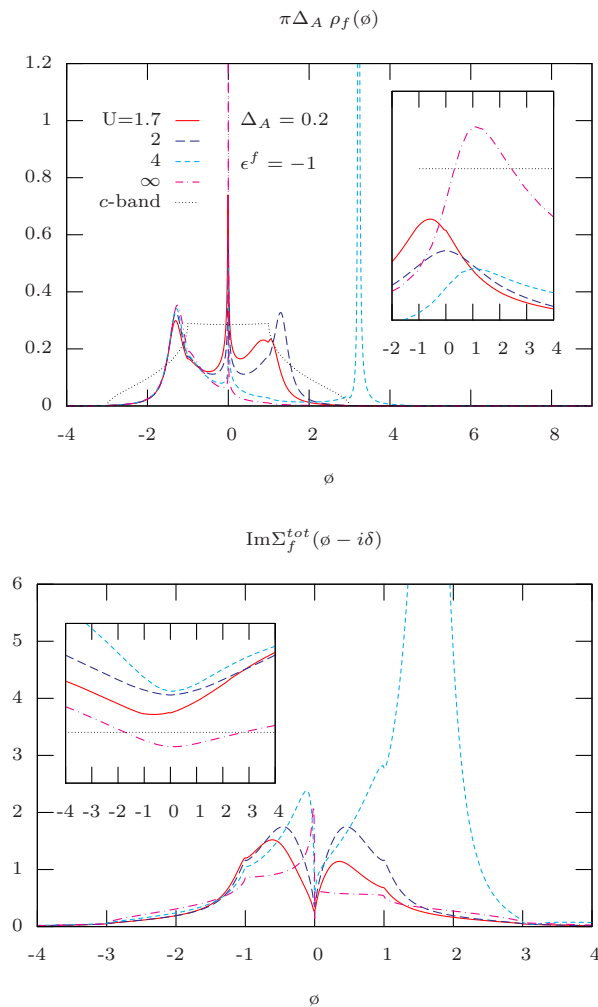


FIG. 3: Rescaled f -electron spectra (upper graph) and total self-energy (lower graph) as a function of energy for various values of the Coulomb repulsion U . The temperature was fixed at half the Kondo temperature $T \approx T_K/2$ of each case, the ionic level was chosen $\epsilon^f = -1$ and the Anderson width was $\Delta_A = 0.2$. The conduction band DOS was that of a three-dimensional tight binding lattice with half bandwidth $W = 3$ (“ c -band” in the upper graph). The insets show the low energy interval around the Fermi level, where the energy is measured in units of the corresponding Kondo temperature and the horizontal lines indicate the $T = 0$ limiting values.

III. RESULTS

As it is well known, the SIAM exhibits the Kondo effect for sufficiently large Coulomb repulsion U and the single particle level below the Fermi energy, $\epsilon^f < 0$. A very prominent manifestation of that effect is the emergence of the Abrikosov-Suhl resonance (ASR) in the one-particle density of states (DOS) at the Fermi level for temperatures of the order of the Kondo temperature T_K . Within the ENCA an order of magnitude estimation for

T_K is given by²⁵

$$T_K = \frac{\min(W, U)}{2\pi} \sqrt{J} e^{-\pi/J}, \quad J = -\frac{2U\Delta_A}{\epsilon^f(\epsilon^f + U)} \quad (31)$$

where J is the effective antiferromagnetic Schrieffer-Wolff exchange coupling, the Anderson width $\Delta_A = \pi\rho_c(0)V^2$ and W the half bandwidth of the conduction electron DOS $\rho_c(\omega)$. The hybridization matrix element was assumed to be local, i.e. momentum independent $V_{\mathbf{k}} \rightarrow V$.

As already mentioned, the pathology of the (S)NCA manifests itself in the overestimation of the height of the ASR and a violation of Fermi liquid properties for too low temperatures as well as in situations with large valence fluctuations^{27,34,35,46}. This pathological behavior is strongest for the case of a spin-only orbital degeneracy ($N = 2$), which is considered in this work. Figure 3 shows the one-particle f -electron DOS $\rho_f(\omega) = \frac{1}{\pi} \text{Im} F_\sigma(\omega - i\delta)$ and the imaginary part of the total self-energy $\text{Im} \Sigma_f^{tot}(\omega - i\delta) = -\text{Im}[1/F_\sigma(\omega - i\delta)]$ calculated within the ENCA and the NCA ($U = \infty$). As can be seen, the ENCA does not overestimate the height of the Kondo peak or violate the Fermi liquid property of the total self-energy $\text{Im} \Sigma_f^{tot}(0 - i\delta) \geq \Delta_A$ down to temperatures of half the Kondo temperature. In contrast, the $U = \infty$ NCA curves in the graphs do violate these limits for the same parameter values. The fact that the ENCA performs better than the NCA in comparable situations is a consequence of a better balance between different kinds of perturbational processes. The importance of such a balance has been pointed out repeatedly^{26,49,50}. Even though the performance of the ENCA is considerably enhanced over the NCA, it eventually overestimates the height of the ASR for even lower temperatures and still misses to produce the correct $T = 0$ Fermi liquid relations. Further improvements can be archived via the incorporation of higher-order diagrams²⁶.

A. Static susceptibilities in the symmetric case

In order to obtain a better understanding of possible shortcomings of the ENCA it is worthwhile to consider charge and spin excitations separately and benchmark them against some exactly known results. The thermodynamics of the SIAM can be obtained exactly from the Bethe ansatz method^{3,4,51,52,53}. At zero temperature and for the symmetric case ($\epsilon^f = -\frac{U}{2}$) with a flat conduction band of infinite bandwidth ($W \rightarrow \infty$) the static susceptibilities can even be obtained in closed form^{53,54},

$$\chi_{mag}^{exact}(T=0) = \frac{(g\mu_B)^2}{4T_L} \left(1 + \frac{1}{\sqrt{\pi}} \int_0^{\frac{\pi\Delta_A}{2U}} dx \frac{\exp\{x - \frac{\pi^2}{16x}\}}{\sqrt{x}} \right) \quad (32)$$

with

$$T_L = U \sqrt{\frac{\Delta_A}{2U}} \exp \left\{ -\frac{\pi U}{8\Delta_A} + \frac{\pi \Delta_A}{2U} \right\} \quad (33)$$

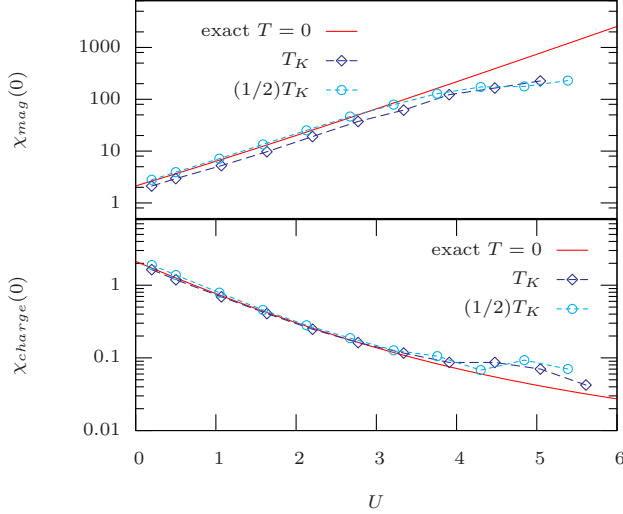


FIG. 4: Static magnetic (upper) and charge (lower) susceptibility for the symmetric case $\epsilon^f = -U/2$ as a function of U for finite temperatures T_K and $T_K/2$ in comparison to the exact $T = 0$ results of equations (32) and (34). The calculations were done for a constant c -electron DOS with half bandwidth $W = 10$ and an Anderson width $\Delta_A = 0.3$.

and

$$\chi_{charge}^{exact}(T=0) = \frac{1}{\pi} \sqrt{\frac{2}{U\Delta_A}} \int_{-\infty}^{\infty} dx \frac{e^{-\frac{\pi\Delta_A}{2U}x^2}}{1 + \left(\frac{U}{2\Delta_A} + x\right)^2} \quad (34)$$

Apart from the small coupling correction $\sim \frac{\Delta_A}{U}$ in the exponent, T_L exactly coincides with the Kondo temperature of equation (31).

In the graphs of Figure 4 the exact zero temperature magnetic (upper) and charge (lower) susceptibilities of equations (32) and (34) (solid red lines) are compared to the ENCA susceptibilities (blue dots) for $\epsilon^f = -U/2$ as a function of U . For the ENCA curves two characteristic temperatures T_K and $T_K/2$ are chosen. The characteristic exponential U dependence of the magnetic susceptibility is essentially the same as for the exact Bethe ansatz result, but the absolute height is somewhat different. For $T = T_K$, the magnetic susceptibility is still reduced, which is certainly expected since then the susceptibility has reached roughly 70% of its saturation value. At half the Kondo temperature the susceptibility has saturated and the agreement is generally quite good. The deviations for $U > 4$ are due to the method used to extract the static susceptibilities: The static limit is obtained by evaluating the dynamic susceptibility at a small but finite external frequency, in our case $\nu = 10^{-5}$. Since the ENCA represents a conserving approximation, the results obtained with this method agree with the static susceptibility obtained from a derivative of a thermodynamic po-

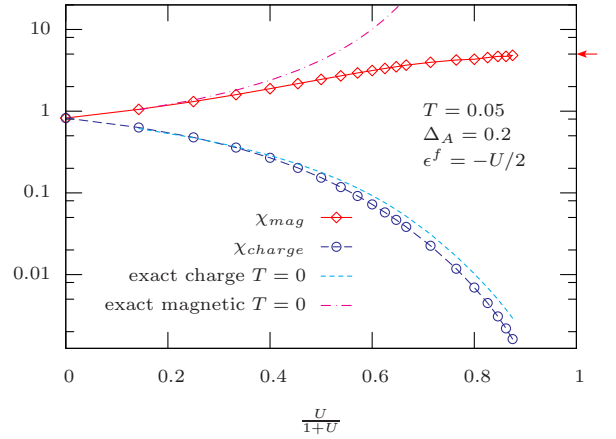


FIG. 5: Magnetic and charge susceptibilities for the symmetric situation ($\epsilon^f = -U/2$) as functions of the Coulomb interaction U at a fixed temperature $T = 0.05$ and for an Anderson width $\Delta_A = 0.2$. Notice, the x -axis is scaled as $U/(1+U)$, so that $U = \infty$ corresponds to $U/(1+U) = 1$. The arrow on the right of the figure corresponds to the value of a Curie susceptibility $\chi_{mag}/(g\mu_B)^2 = 1/(4T) = 5$ of a free spin at temperature $T = 0.05$.

tential, or solving separate equations as in Otsuki et al.⁵⁵. This is valid as long as the minimal frequency is negligible compared to the lowest energy scale in the problem. However, the Kondo temperature for $U = 4$ is only of the order of 10^{-4} and decreases for larger U . The susceptibility calculated at $\nu = 10^{-5}$ does then no longer represent the static limit anymore, and the decrease seen in Figure 4 is produced, which is therefore not indicating a shortcoming of the ENCA method. The deviation can be cured by choosing a smaller value for the external frequency.

The charge susceptibility (lower graph in Figure 4) shows no significant temperature dependence for $T = T_K$ and $T_K/2$ and lies right on top of the exact $T = 0$ result. The deviations for $U \geq 4$ are explained in the same way as for the magnetic susceptibility described above.

These reasons for the deviation at larger U can be further confirmed by calculating the static susceptibilities for a fixed finite temperature $T = 0.05$ as a function of the Coulomb interaction, which are shown in Figure 5. Again the figure compares the static magnetic (red dots) and charge (blue dots) susceptibilities for the symmetric situation with the exact $T = 0$ results. The charge susceptibility is a monotonically decreasing function with increasing Coulomb repulsion as it is expected; it very accurately follows the exact zero temperature susceptibility, which again confirms its weak temperature dependence in symmetric situations at low temperatures. The magnetic susceptibility (red dots) does agree with the exact $T = 0$ solution for low Coulomb repulsions but deviates for $U/(1+U) \gtrsim 1/3$ ($U \gtrsim 1/2$). This is a finite temperature effect, since for values of $U \gtrsim 1/2$ the Kondo tem-

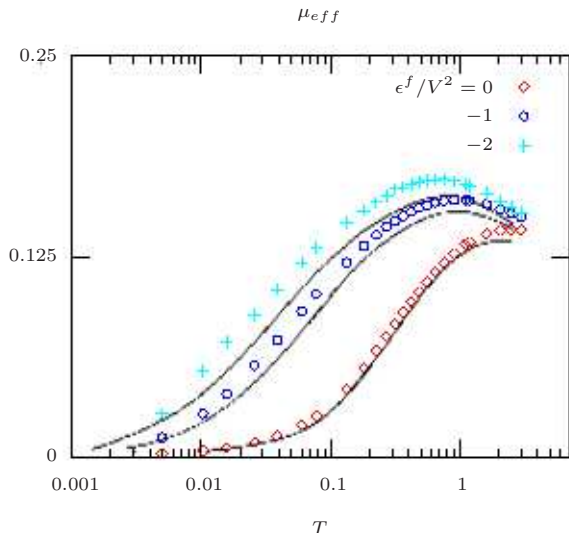


FIG. 6: Temperature dependent effective magnetic moment within the ENCA (colored dots) for a fixed Coulomb repulsion $U = 4V^2$ and three different f -level positions $\epsilon^f = 0, -V^2, -2V^2$. The solid grey curves are the exact Bethe ansatz results for the same parameter values (after Okiji and Kawakami⁵⁶). The calculations were done for a constant c -electron DOS with half bandwidth $W = 10$ and $\Delta_A = 0.167$.

perature is smaller than the chosen finite temperature of $T = 0.05$. Consequently, for $U \gtrsim 1/2$ we are not in the low temperature regime and the susceptibility is not well described by its $T = 0$ value. The magnetic susceptibility does not grow exponentially with U as for $T = 0$, but instead saturates for $U \rightarrow \infty$ at the asymptotic value of the Curie susceptibility of a free spin, $\chi_{mag} = 1/(4T) = 5$, which is indicated by an arrow on the right border of the graph.

B. Static susceptibilities in the asymmetric case

As a first test for the ENCA in the asymmetric situation Figure 6 compares the effective screened local magnetic moment of the impurity,

$$\mu_{eff} = \frac{1}{(g\mu_B)^2} T \chi_{mag}(\nu = 0) \quad , \quad (35)$$

to the exact Bethe ansatz results for three different ionic level positions as a function of temperature. The solid grey lines are the exact Bethe ansatz solution, which is taken from Okiji and Kawakami⁵⁶, while the colored points are ENCA calculations for the same parameter values. The half bandwidth was taken to be $W = 10$, which should be large enough in order to be comparable to the Bethe ansatz solution with $W = \infty$. The overall trend of the ENCA is to slightly overestimate the effective moment but all characteristic features are essentially

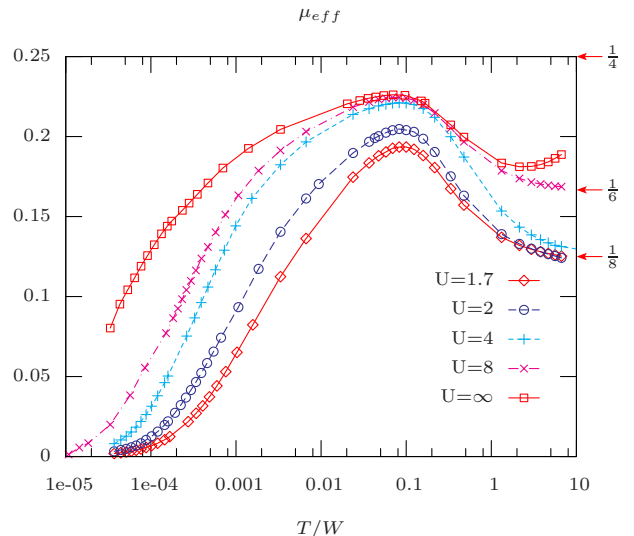


FIG. 7: Temperature dependent screened local moment μ_{eff} for various Coulomb repulsions U . The conduction band is modeled by three dimensional simple cubic (3d-SC) DOS with half bandwidth $W = 2t = 3$, the Anderson width is $\Delta_A = 0.2$ and $\epsilon^f = -1$ for all cases considered. The arrows on the right border of the graph denote the asymptotic values in the free orbital ($1/8$), valence fluctuation ($1/6$) and local moment ($1/4$) regimes.

the same as for the Bethe ansatz. Especially the shape and the relative height of the curves is in remarkable agreement: All three ENCA curves can be brought to lie right on top of the exact Bethe ansatz results when they are rescaled with one single factor. This indicates that the ENCA produces only a slightly modified Kondo scale, but otherwise describes the static magnetic properties almost exactly. This is especially remarkable for the intermediate valence situation with $\epsilon^f = 0$, where the empty and singly occupied ionic configurations are almost degenerate. In such situations stronger pathologies occur in the one-particle DOS and the NCA-type of approximations would be expected to yield results of lower quality. However, as it can be seen, the magnetic excitations are still described very accurately.

The effective local moment for various Coulomb repulsions U as a function of temperature is displayed in Figure 7 for an impurity embedded into a three dimensional simple-cubic (3d-SC) band of conduction electrons (half bandwidth $W = 2t = 3$). The local f -moment tends to zero for low temperatures in all cases and the general shape of the curves resembles the exact solutions known from the literature^{7,8,53}. The values of the local moment in the different asymptotic regimes, indicated by the arrows on the right border of the graph, are clearly visible: At high temperatures the impurity is effectively non-interacting and the susceptibility is $1/(8T)$ due to the induced moment (free orbital regime, $\mu_{eff} = 1/8$).

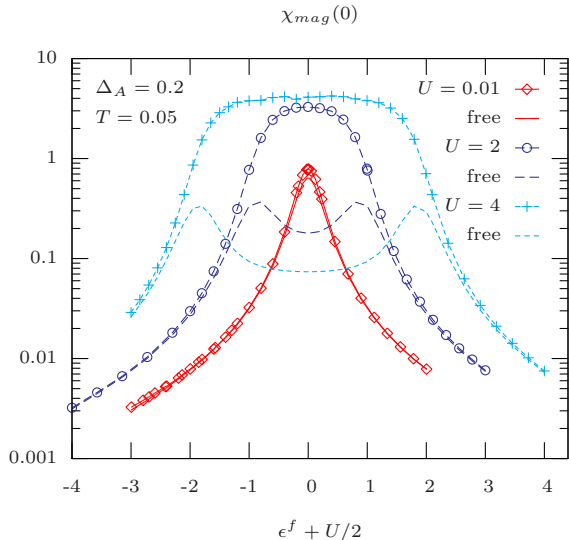


FIG. 8: Static magnetic susceptibility for a fixed $T = 0.05$ and $\Delta_A = 0.2$ as functions of the ionic level position ϵ^f relative to the half-filling value $-U/2$ for various values of U . The conduction band was chosen to be constant with a half bandwidth of $W = 10$. Curves without dots (“free”) are calculated without two-particle interactions, i.e. with the particle-hole propagator of equation (36).

For lower temperatures the effect of the Coulomb repulsion becomes noticeable and leads to a depopulation of empty and doubly occupied f -states, which results in the formation of a local f -spin along with an increased effective moment (local moment regime, $\mu_{eff} = 1/4$). As the temperature is still lowered, Kondo physics comes into play and the local f -spin is increasingly screened, eventually leading to a vanishing effective moment (strong coupling regime, $\mu_{eff} = 0$). The tendency to form a local moment is stronger for larger values of U , and it persists to lower temperatures before the Kondo-screening sets in. This is especially true for the cases of $U = 4$ and $U = 8$, where the upper Hubbard peak lies outside the c -band and direct hybridization processes involving the doubly occupied f -states are strongly suppressed. In the asymmetric case, the valence fluctuation regime with $\mu_{eff} = 1/6$ can be traversed as seen in the curves for $U = 8$, where again the upper Hubbard peak is irrelevant due to the lack of hybridization processes even at high temperatures. The upturn in the $U = \infty$ moment around $T/W \geq 2$ is due to numerical deficiencies and should not be taken as a physical tendency.

In order to examine the magnetic susceptibility as a function of the ionic level position ϵ^f in more detail, Figure 8 shows $\chi_{mag}(0)$ for fixed T and U , but as functions of ϵ^f relative to the value for half filling $-U/2$. Also shown are the susceptibilities without explicit two-particle interactions (lines without dots labeled as “free”), i.e. the

local particle-hole propagator $P^f(0)$ calculated via

$$P^f(\nu) = \int_{-\infty}^{\infty} d\omega f(\omega) \rho_f(\omega) \quad (36)$$

$$\times [F_{\uparrow}(\omega + \nu + i\delta) + F_{\uparrow}(\omega - \nu - i\delta)] \quad ,$$

where F_{\uparrow} represents the one-particle f -Green function (cf. equation (9)), $\rho_f(\omega)$ the corresponding spectrum and $f(\omega)$ the Fermi function. The first thing to notice is that all curves are symmetric around $\epsilon^f + \frac{1}{2}U = 0$, which just reflects the particle-hole symmetry of the model. The particle-hole propagators shows the expected maxima approximately situated at the positions of the Hubbard peaks in the one-particle DOS $\epsilon^f + \frac{1}{2}U \approx \pm \frac{1}{2}U$. For very small $U = 0.01$, the susceptibility calculated with the ENCA is indistinguishable from the particle-hole propagator, as a consequence of the near lack of two-particle correlations. The ENCA susceptibility shows only one broad maximum around $\epsilon^f + \frac{1}{2}U = 0$ (half filling), which increases in height and width for larger values of U . The enhancement of the susceptibility is due to the increasing local magnetic moment with larger U . The plateau which develops around zero, is due to the stability of the local moment as long as the singly occupied ionic configuration is stable, i.e. the lower Hubbard peak being below and the upper above the Fermi level, and the temperature is not too low compared to T_K . But as soon as one of the Hubbard peaks extends over the Fermi level, i.e. $\epsilon^f + \frac{1}{2}\Delta_A < 0$ or $\epsilon^f + U - \frac{1}{2}\Delta_A > 0$, the moment is destabilized. For both Hubbard peaks below (above) the Fermi level, the impurity is predominantly doubly occupied (empty) and the magnetic susceptibility drops drastically. The curve then rapidly approaches the particle-hole propagator, indicating that explicit two-particle interactions are unimportant.

The temperature dependent static charge susceptibility is shown in the Figure 9 for various values of U as a function of temperature. For high temperatures and $U < 4$ the static susceptibility behaves effectively non-interacting with $\chi_{charge} = 1/(8T)$ as expected. For $U = 4$ the susceptibility still has the characteristic $1/T$ dependence for high T , but with a prefactor more closely to $1/16$. This can be understood since in this situation the upper Hubbard peak (incorporating roughly half the spectral weight) is energetically just above the upper band edge of the c -band and therefore the accessible spectral weight for two-particle excitations is approximately halved. The rapid drop of the susceptibility for $U = 4$ at temperatures $T \gtrsim W$ is attributed to inaccuracies in the numerics for solving the integral equations. However, in this effectively non-interacting regime the susceptibility can be calculated without explicit two-particle interactions via the particle-hole propagator of equation (36). The results thus obtained are shown in the graph as colored dots without joining lines and are seen to be nicely proportional to $1/T$ for high temperatures.

At temperatures around $T/W \approx \frac{1}{3}$ all susceptibilities show a pronounced maximum, which stems from

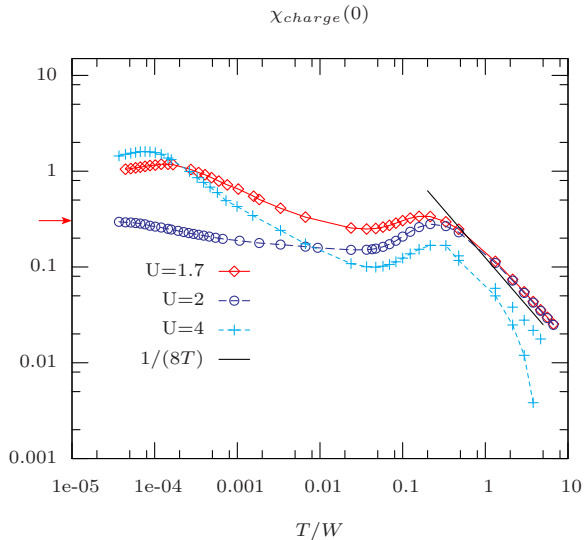


FIG. 9: Temperature dependent static charge susceptibility $\chi_{charge}(0)$ for various Coulomb repulsions U ($\Delta_A = 0.2$, $\epsilon^f = -1$). The arrow at the left border shows the exact $T = 0$ limit for the symmetric case $U = 2$. The high temperature asymptotic form of a non-interacting impurity ($\chi = 1/(8T)$) is shown as well (thick line). The colored dots, which are not connected by a line, denote the asymptotic susceptibilities calculated without any two-particle interactions, i.e. from $P^f(\nu = 0)$, see equation (36). The conduction band was chosen to be that of a 3d-SC lattice with a half bandwidth of $W = 3$.

thermally excited charge fluctuations between the empty and singly occupied ionic levels with excitation energy $\approx |\epsilon^f|/W = 1/3$. For $U = 2$, fluctuations between the singly and doubly occupied states have the same excitation energy $|\epsilon^f|/W = (\epsilon^f + U)/W = 1/3$ and therefore contribute equally. For $U = 1.7$ the energy of fluctuations involving the doubly occupied state is somewhat smaller ($\sim \frac{0.7}{3} \approx 0.23$) and the peak is therefore broadened to lower energies. For $U = 4$ the doubly occupied state is inaccessible for thermal fluctuations; so only the empty and singly occupied levels contribute leading to a reduction of the susceptibility maximum by approximately a factor of two.

At lower temperatures ($T/W \leq 0.05$ in the figures) the charge susceptibilities exhibit a slow increase followed by a saturation at the zero temperature values. The increase in the charge susceptibility occurs in a temperature range, where the Kondo singlet and the local Fermi liquid formation take place, which manifests itself in the growing many-body resonance at the Fermi level in one-particle DOS $\rho_f(\omega)$. Even though a direct interpretation of the increase in terms of a Fermi liquid picture (where the charge susceptibility is proportional to the DOS at the Fermi level) is not applicable since the Fermi liquid is formed only at very low temperatures, it still provides

an intuitive way of understanding: The increasing spectral weight at the Fermi level leads to an enlarged phase space volume for two-particle excitations and the charge susceptibility is at least roughly proportional to the DOS at the Fermi level. This is supported by the fact, that $\chi_{charge}(0)$ increases logarithmically with decreasing temperature, which is also the case for $\rho_f(0)$. But how strong the increase actually is and how it is influenced by the value of the Coulomb repulsion U cannot be deduced from the simplified Fermi liquid analogy. This rather depends on the details of the two-particle correlations. In the symmetric situation ($U = -2\epsilon^f = 2$) the charge susceptibility increases only moderately and approaches the exact $T = 0$ limiting value known from the Bethe ansatz, which is indicated by the arrow at the left border of the Figure 7. For the asymmetric cases, the increase is considerably more pronounced. Especially, the drastic low temperature increase for $U = 4$ is rather unexpected. The absolute value of the susceptibility is even larger than for the smaller values of U , which is counter-intuitive since charge fluctuations should be suppressed for larger U . However, the tendency that for a given level position ϵ^f the charge susceptibility in the asymmetric situation can increase with growing U is known from perturbation theory⁵⁷ as a characteristic feature of valence fluctuation physics. Valence fluctuations being at the origin of this enhanced low temperature increase of the charge susceptibility are in agreement with the observation already made above, that for $U = 4$ the doubly occupied ionic orbital is outside the conduction band and the system is therefore from the outset closer to the intermediate valence fixed point.

Reference calculations with the NRG (not shown) indeed display the characteristic features of the charge susceptibility as shown in Figure 9: A maximum for temperatures of the order of the ionic level positions $|\epsilon^f|$ and $\epsilon^f + U$ and an increase towards lower temperatures. In situations close to the valence fluctuation regime this increase leads to an enhancement of the charge susceptibility by a factor of about 10. However, the parameter values chosen for the $U = 4$ ENCA-curve are not very close to the valence fluctuation fixed point. This is also reflected in the magnetic susceptibility for $U = 4$, which does not show any signatures of the valence fluctuation regime, but rather exhibits behavior characteristic for the transition from a local moment to the strong coupling fixed point. NRG calculations with parameter values similar to the ones chosen in this study, did show a low temperature increase, but not as strong as observed with the ENCA. Altogether it can be concluded, that the ENCA does describe the charge fluctuations qualitatively right, but overestimates the influence of intermediate valence phenomena at very low temperatures in the asymmetric case.

To make the range of applicability of the ENCA more clear, it is instructive to consider the charge susceptibility for fixed values of U and T , varying the ionic level positions ϵ^f , which is shown in Figure 10. The particle-hole

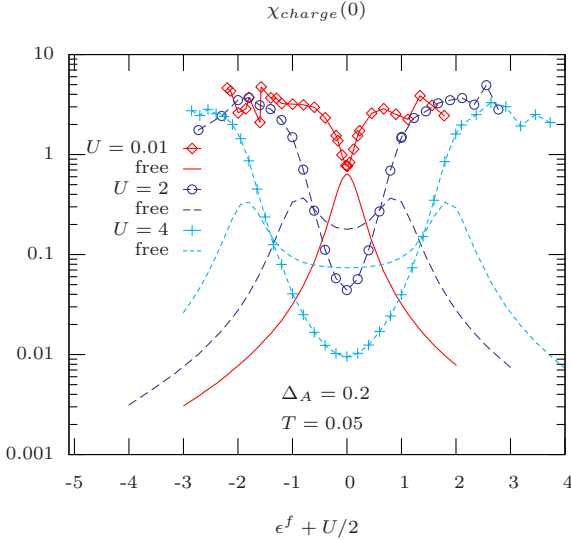


FIG. 10: Static charge susceptibility for a fixed $T = 0.05$ and $\Delta_A = 0.2$ as functions of the ionic level position ϵ^f relative to the half-filling value $-U/2$ for various values of U . The conduction band was chosen to be constant with a half bandwidth of $W = 10$. Curves without dots (“free”) are calculated without two-particle interactions, i.e. with the particle-hole propagator of equation (36).

propagators already displayed in Figure 8 are included as well (lines without dots). The ENCA charge susceptibilities are always minimal for half filling ($\epsilon^f + U/2 = 0$) and increases away from the symmetric case. The absolute value of the charge susceptibility in the symmetric situation is drastically reduced compared to the corresponding particle-hole propagator for large values $U = 2$ and $U = 4$, which indicates, that the two-particle correlations strongly suppress charge fluctuations. In that situation, the susceptibility cannot accurately be described by the one-particle DOS alone and assuming independent though strongly renormalized quasiparticles. On the logarithmic scale, the increase with growing distance from zero can nicely be fitted with a parabola centered at zero, which corresponds to an exponential increase of the susceptibility, $\chi_{charge} \sim e^{\alpha(\epsilon^f + U/2)^2}$, ($\alpha > 0$). This shows the strong influence of the asymmetry and the contribution of valence fluctuations to the charge fluctuations. However, the ENCA clearly fails for large asymmetries as the susceptibility saturates for $|\epsilon^f + \frac{1}{2}U| > \frac{1}{2}U^{68}$. Contrary to that, $\chi_{charge}(0)$ should decrease again (cf. Horvatic and Zlatić⁵⁷ or Schlottmann⁵⁸) and approach the particle-hole propagator, due to the effective non-interacting nature. This is most drastic for the almost non-interacting case with $U = 0.01$, where, apart from reproducing the value at half filling quite accurately, the curve goes the opposite direction as expected. The values at which the downturn in the susceptibility should occur correspond to situations, where both Hubbard peaks in

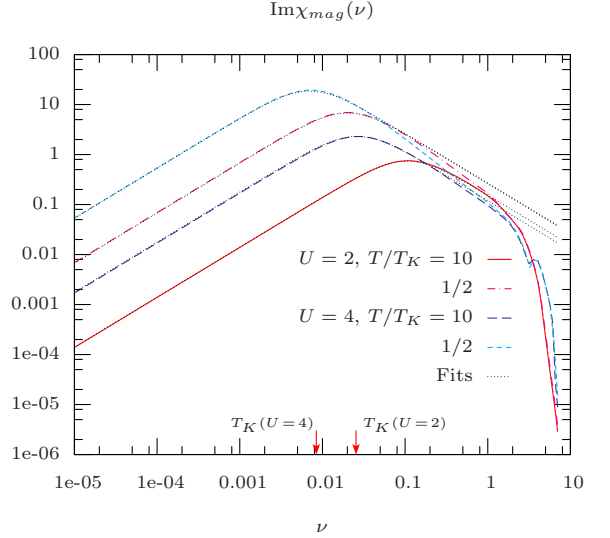


FIG. 11: The imaginary part of the dynamic magnetic susceptibility for $\epsilon^f = -1$ two values of U ($U = 2, 4$) and two characteristic temperatures ($T = 10T_K, T_K/2$) in a double-logarithmic plot. The corresponding Kondo temperatures are indicated as arrows on the frequency axis. All curves are calculated for $\Delta_A = 0.3$ and a 3d-SC band DOS ($W = 3$).

the one-particle spectrum (very roughly at ϵ^f and $\epsilon^f + U$) are either below or above the Fermi level, corresponding to the empty- and fully occupied impurity regimes. Since ENCA is designed to describe spin flip scattering and the magnetic exchange coupling correctly, it does not fully capture the physics of charge fluctuations outside the Kondo regime. In situations, where the unperturbed ground state is either the empty or doubly occupied ionic state, crossing diagrams neglected in the ENCA are vital to describe charge fluctuations accurately. On the other hand magnetic fluctuations are still described very accurately in these situations (see Figures 6 and 8).

C. Dynamic susceptibilities

After discussing the range of validity of the ENCA by means of the static susceptibilities, we will now turn to the description of dynamic magnetic and charge fluctuations. The imaginary part of the dynamic magnetic susceptibility is shown in Figure 11 for two different values of U and two characteristic temperatures. The spectrum of the susceptibility shows a pronounced maximum, which is shifted to lower frequencies and increases considerably in height as the temperature is lowered. For temperatures below the Kondo temperature, the position of the maximum remains fixed at a value of the order of the Kondo temperature. Also shown in the figure are fits

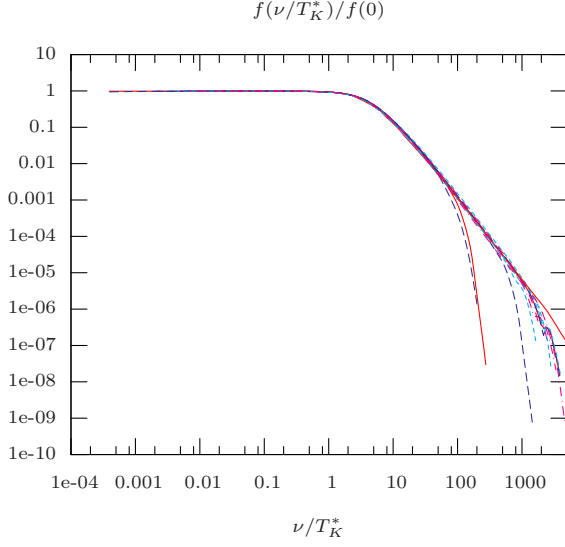


FIG. 12: Scaling function $f(\nu/T_K^*)/f(0)$ from equation (38) for the following parameter sets: $(\epsilon^f = -0.5; U = 1; T/T_K = 10, 1)$, $(\epsilon^f = -1; U = 2; T/T_K = 1)$, $(\epsilon^f = -1.5; U = 3; T/T_K = 1)$, $(\epsilon^f = -2; U = 4; T/T_K = 1)$, $(\epsilon^f = -1; U = 3; T/T_K = 1)$, $(\epsilon^f = -1; U = 4; T/T_K = 1, 1/2, 1/3, 1/5, 1/7, 1/10)$ and $(\epsilon^f = -1; U = 8; T/T_K = 1)$. All curves are calculated for $\Delta_A = 0.3$ and a 3d-SC band DOS.

with a Lorentzian form

$$\chi_{mag}^{fit}(\nu) = \frac{\chi_0}{1 - i\nu/\Gamma} \quad , \quad \nu \in \mathbb{R} \quad , \quad (37)$$

which describe the low frequency susceptibilities very well. The form (37) for the magnetic susceptibility corresponds to an exponential spin relaxation with relaxation time $1/\Gamma$. The line-width Γ is directly proportional to the NMR impurity nuclear spin-lattice relaxation rate $\Gamma \sim T_1^{59}$. The relaxation rates Γ extracted from susceptibilities for various parameters follows a \sqrt{T} -law²⁴ for high temperatures and saturates at a value of the order of T_K at temperatures below T_K (not shown), in accord with what was already found earlier^{29,60,61}. The physical picture behind these findings is quite clear: Upon lowering the temperature, the local moment of the impurity becomes increasingly coupled to the surrounding spin of the band electrons resulting in an enhanced response. At temperatures of the order of or lower than the Kondo temperature, the local Fermi liquid state is approached in which the local spin is screened and a local Kondo singlet is formed with a “binding energy” of about T_K . Therefore the maximum in the spin excitations spectrum, as well as the NMR relaxation rate, both are pinned at an energy of the order of T_K .

Jarrell et al.⁶¹ also found that the function

$$f(\nu) = \frac{\pi T_K}{2\chi_{mag}(0)} \frac{\text{Im}\chi_{mag}(\nu)}{\nu} \quad (38)$$

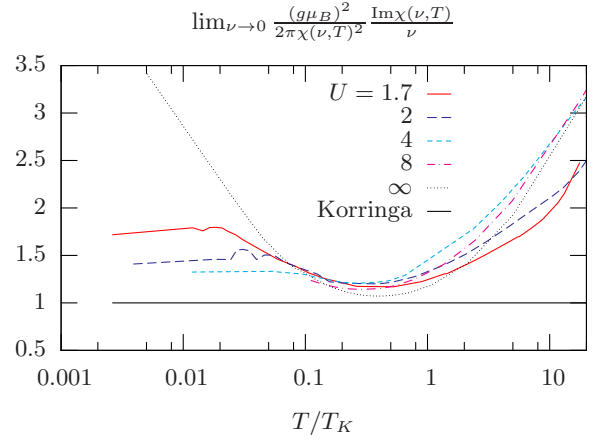


FIG. 13: $\lim_{\nu \rightarrow 0} \frac{(g\mu_B)^2}{2\pi\chi_{mag}(\nu,T)^2} \frac{\text{Im}\chi_{mag}(\nu,T)}{\nu}$ evaluated as a function of temperature and various Coulomb repulsions within the ENCA. For comparison the $U = \infty$ -NCA curve is shown as well. A 3d-SC DOS was used for the conduction electrons and $\Delta_A = 0.3$.

shows universality and depends only on T/T_K . Figure 12 shows this function normalized to its zero frequency value for various parameter sets. All graphs can be collapsed onto one single curve showing the universal shape of the function f for low energies. In order to achieve scaling a guess for the actual Kondo temperature T_K^* has to be used. In contrast, the T_K -value calculated by equation (31) and used in this work does not represent the exact physical low energy scale T_K^* , but only provides an order of magnitude estimate. The value of the “real” Kondo temperature could have been extracted from fits of the calculated susceptibilities to the universal curve of the susceptibility as described by Jarrell et al.⁶². The rapid decrease of the curves in the figure for frequencies of $\nu/T_K^* \gtrsim 100$ stems from the finite bandwidth of the 3d-SC conduction band used for these calculations. Additionally, non-universal corrections stemming from the shape of the band DOS are also a reason why the absolute height of the functions $f(\nu)$ did not obey exact universality and had to be renormalized to their zero frequency value $f(0)$ (the $f(0)$ are all of the order of one).

The above findings clearly confirm, that the dynamics of the impurity spin is solely determined by the antiferromagnetic exchange between the impurity- and conduction electron spins. Even in the asymmetric situation, the only relevant energy scale for magnetic fluctuations of the impurity is the Kondo temperature T_K at low temperatures.

As it was already mentioned earlier, the NCA does violate Fermi liquid properties for very low temperatures. Another indication, in addition to the imbalance of the imaginary part of the total self energy at the Fermi level ($-\text{Im}\Sigma(0+i\delta) < \Delta_A$), stems from the zero frequency limit of the imaginary part of the dynamic susceptibility. For

the Fermi liquid at $T = 0$ it has to obey the so called Korringa-Shiba relation⁵⁹

$$\lim_{\nu \rightarrow 0} \frac{(g\mu_B)^2}{2\pi\chi_{mag}(\nu)^2} \frac{\text{Im}\chi_{mag}(\nu)}{\nu} = 1 \quad . \quad (39)$$

The function on the left hand side of this relation is shown in Figure 13 as a function of temperature for various values of U . For the NCA, the quantity $\lim_{\nu \rightarrow 0} \text{Im}\chi_{mag}(\nu)/\nu$ is known to diverge at $T = 0$ ⁶³, which is reproduced by the $U = \infty$ curve in the figure. However, the ENCA (finite U values) performs considerably better than the NCA. The curves still fall short of reproducing the exact limit and even slightly increase for temperatures $T \lesssim T_K/2$, but they eventually saturate at a finite value and do not diverge. This represents a considerable improvement of the qualitative behavior of the ENCA over the NCA.

The imaginary part of the dynamic charge susceptibilities for two different Coulomb repulsions and characteristic temperatures, calculated with a 3d-SC band DOS, are shown in Figure 14. In the spectra the characteristic features stemming from excitations involving the Hubbard peaks at energies around $|\epsilon^f|$ and $\epsilon^f + U$ are clearly visible. In the symmetric case ($U = 2$), the height of the peak at $\nu \approx |\epsilon^f|$ is about twice of the one in the asymmetric case ($U = 4$). This is due to the doubled phase-space volume for the symmetric situation with excitation energies matching, $\epsilon^f + U = |\epsilon^f|$, while for $U = 4$ the upper Hubbard peak is moved to higher energies.

Also shown in the graphs are the local particle-hole propagators of equation (36) (labeled as “free”). These show characteristic features of the Hubbard peaks too, but the most prominent difference to the fully interacting susceptibility is the strong suppression of the high energy response in the latter. For example, the broad excitation continuum in the particle-hole propagator of the asymmetric case ($U = 4$) for energies in the range $3 \leq \nu \leq 6$ is reduced to a very small peak at $\nu \approx 3$ in the fully interacting susceptibility. $P^f(\nu)$ is just a measure for the phase space volume for statistical independent particle-hole excitations, which are described by the one-particle DOS ρ_f . The strongly renormalized quasiparticles and -holes at the Fermi level, on the other hand, are strongly correlated, leading to an effective suppression of the available phase space volume. The role of the low energy quasiparticles can be studied by comparing the particle-hole propagator and the interacting susceptibilities at low energies for the symmetric situation ($U = 2$, inset). The response via the particle-hole propagator for $\nu \leq T_K$ shows an increase for lower temperatures, which stems from the quasiparticle-quasihole excitations within the growing Kondo resonance. In the fully interacting susceptibility this increase is approximately an order of magnitude smaller, clearly showing the effect of correlations in the two-particle response. Surprisingly, for the asymmetric case ($U = 4$) this trend is reversed and the interacting susceptibility is enhanced over the particle-hole propagator for excitation energies smaller than the Kondo scale

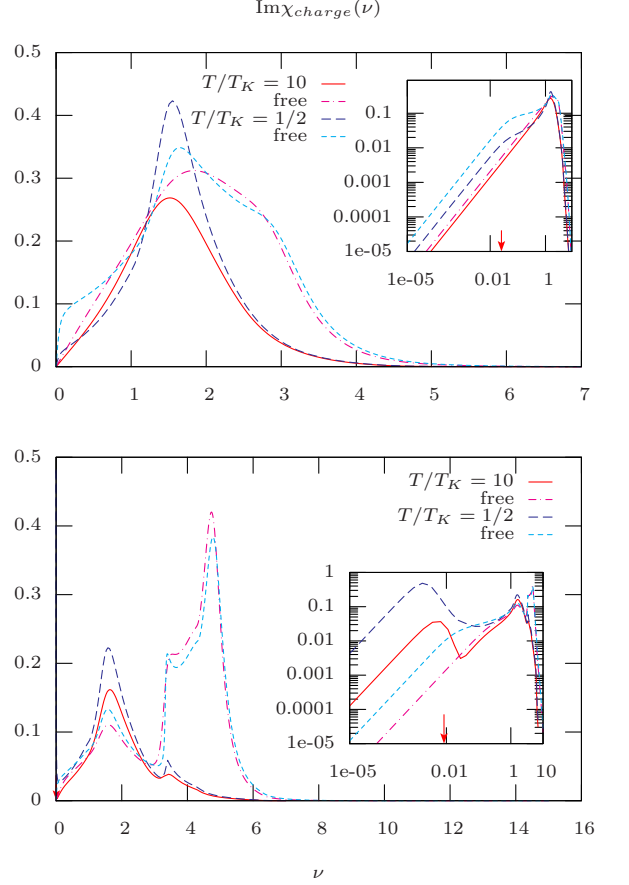


FIG. 14: Imaginary part of the dynamic charge susceptibility for the symmetric ($\epsilon^f = -1$, $U = 2$, upper) and asymmetric ($\epsilon^f = -1$, $U = 4$, lower) case for two characteristic temperatures $T = 10T_K$ and $T = T_K/2$. The curves for the particle-hole propagators (“free”) are shown as well. The insets show the corresponding low energy region on a double-logarithmic scale. The Kondo temperature for each case is indicated by the red arrow on the frequency axis in the low energy insets. The calculations are done for a 3d-SC band and $\Delta_A = 0.3$.

$\nu \leq T_K$ (see inset). This very pronounced low energy response is produced by quasiparticle-quasihole excitations in the local Fermi liquid phase at low temperatures. The fact that these excitations are strongly enhanced in the asymmetric case compared to the symmetric situation is associated with the presence of strong valence fluctuations, as was already discussed for the static susceptibility above. Even though such a low energy enhancement was not reported in NRG calculations for the charge susceptibility^{37,64} an inspection of the low energy part of the many-body spectrum obtained with the NRG⁶⁵ and preliminary NRG-calculations indeed suggest the possibility of an enhanced charge response for asymmetric situations. Additionally, a similar but not so strong temperature dependent increase in the dynamic susceptibility for temperatures of the order of the Kondo tempera-

ture was already found for larger orbital degeneracy and $U = \infty$ with the NCA⁴⁸. Therefore we argue, that these findings for the dynamic charge susceptibility are in accord with the ones discussed in the previous section for the static charge susceptibility. The observed increase of the charge response for energies smaller than the Kondo scale is indeed physical and due to the influence of the valence fluctuations of the low temperature Fermi liquid. However, the magnitude of the enhancement shown in Figure 14 is arguable, especially for the choice of parameters in the present calculation.

IV. CONCLUSIONS

We have studied the SIAM within a conserving approximation, the ENCA, for a variety of model parameters. It was shown, that the ENCA constitutes a very accurate approximation for the static and dynamic one- and two-particle quantities of that model for temperatures down to a fraction of the Kondo temperature. It considerably improves the Fermi liquid properties and cures shortcomings of the (S)NCA, like the removal of the divergence of $\lim_{\nu \rightarrow 0} \frac{\text{Im}\chi_{mag}(\nu)}{\nu}$ at zero temperature. In symmetric situations ($2\epsilon^f + U = 0$), the static magnetic and charge susceptibilities were shown to be in excellent agreement with the exact Bethe ansatz results. This was even true for cases with very small Coulomb interaction U , which could not be expected from the beginning, since approximations within direct perturbation theory with respect to the hybridization usually have problems describing the non-interacting case. The static magnetic susceptibility is in excellent agreement with exact Bethe ansatz results in the asymmetric situation. This holds also in cases with strong valence fluctuations, such as for $\epsilon^f = 0$ or in the empty- and fully occupied orbital regimes. However, the static charge susceptibility in the asymmetric model is described accurately only in situations, where the singly occupied impurity valence state represents the unperturbed ($\Delta_A = 0$) ground state. In addition, even though we believe that the qualitative features of the charge susceptibility in asymmetric situations are captured by the presented calculations, the influence of valence fluctuations is probably overestimated for too low temperatures. This confirms the expectation, that crossing diagrams, which are neglected in the ENCA, are essential for the

quantitative description of situations with strong valence fluctuations, where the impurity occupation is statistically fluctuating. This also is in accord with the known pathologies in the one-particle spectral function. There, charge and magnetic fluctuations both contribute and the overestimation of the charge excitations at very low temperatures leads to the overshooting of the Kondo resonance and the observes spikes in the DOS. The dynamic magnetic susceptibility is dominated by Kondo screening of the impurity spin. The ENCA correctly reproduces the temperature and other parameter dependencies of the magnetic excitations, and even the scaling found in previous studies is obtained. The Korringa-Shiba relation is still slightly violated for very low temperatures, but the improvement of the ENCA over the NCA is considerable since the divergence for $T \rightarrow 0$ is removed. The dynamical charge spectrum shows a severe suppression of high energy excitations due to correlations, when compared to the particle-hole propagator, which would represent the susceptibility of independent renormalized quasiparticles. Additionally the low energy response for excitation energies smaller than the Kondo temperature is also strongly suppressed in the symmetric case, due to the same correlations between low energy quasiparticles. However, in the asymmetric situation the low energy charge response is drastically enhanced and an additional peak emerges. This enhancement is attributed to the presence of the valence fluctuation fixed point in the asymmetric model. Such an enhancement seems quite probable so that only the steepness of the increase calculated within the ENCA for parameter values chosen is arguable.

With these findings, the prospects of describing two-particle dynamics of lattice systems within the DMFT are very promising and results will be presented in a subsequent publication²⁴.

Acknowledgments

The authors acknowledge fruitful discussions with E. Jakobi and F.B. Anders. One of us (SS) especially thanks F.B. Anders for providing him with his NRG code to perform the reference calculations mentioned in the text, and acknowledges support from the DFG under Grant No. An245/6-1.

¹ P. W. Anderson, Phys. Rev. **124**, 41 (1961).

² N. Andrei, K. Furuya, and J. H. Lowenstein, Rev. Mod. Phys. **55**, 331 (1983).

³ P. B. Wiegmann and A. M. Tselick, J. Phys. C **16**, 2281 (1983).

⁴ A. M. Tselick and P. B. Wiegmann, J. Phys. C **16**, 2321 (1983).

⁵ A. Tselick and P. Wiegmann, Adv. Phys. **32**, 453 (1983).

⁶ K. G. Wilson, Rev. Mod. Phys. **47**, 773 (1975).

⁷ H. R. Krishna-murthy, J. W. Wilkins, and K. G. Wilson, Phys. Rev. B **21**, 1003 (1980).

⁸ H. R. Krishna-murthy, J. W. Wilkins, and K. G. Wilson, Phys. Rev. B **21**, 1044 (1980).

⁹ R. Bulla, T. Costi, and T. Pruschke, Rev. Mod. Phys. **80**, 395 (2008).

¹⁰ S. R. White, Phys. Rev. Lett. **69**, 2863 (1992).

¹¹ S. R. White, Phys. Rev. B **48**, 10345 (1993).

¹² T. D. Kühner and S. R. White, Phys. Rev. B **60**, 335

- (1999).
- ¹³ K. Hallberg, *Adv. Phys.* **55**, 477 (2006).
 - ¹⁴ J. E. Hirsch and R. M. Fye, *Phys. Rev. Lett.* **56**, 2521 (1986).
 - ¹⁵ A. N. Rubtsov, V. V. Savkin, and A. I. Lichtenstein, *Phys. Rev. B* **72**, 035122 (2005).
 - ¹⁶ P. Werner, A. Comanac, L. de' Medici, M. Troyer, and A. J. Millis, *Phys. Rev. Lett.* **97**, 076405 (2006).
 - ¹⁷ H. Keiter and J. C. Kimball, *J. Appl. Phys.* **42**, 1460 (1971).
 - ¹⁸ H. Keiter and J. C. Kimball, *Int. J. Magn.* **1**, 233 (1971).
 - ¹⁹ N. Grewe and H. Keiter, *Phys. Rev. B* **24**, 4420 (1981).
 - ²⁰ H. Keiter and G. Morandi, *Phys. Rep.* **109**, 227 (1984).
 - ²¹ A. Georges, G. Kotliar, W. Krauth, and M. J. Rozenberg, *Rev. Mod. Phys.* **68**, 13 (1996).
 - ²² S. Schmitt and N. Grewe, *Physica B* **359-361**, 777 (2005).
 - ²³ M. Jarrell, *Phys. Rev. B* **51**, 7429 (1995).
 - ²⁴ S. Schmitt, Ph.D. thesis, TU Darmstadt (2008), URL <http://tuprints.ulb.tu-darmstadt.de/1264/>.
 - ²⁵ T. Pruschke and N. Grewe, *Z. Phys. B* **74**, 439 (1989).
 - ²⁶ N. Grewe, S. Schmitt, T. Jabben, and F. B. Anders, *J. Phys.: Condens. Matter* **20**, 365217 (2008).
 - ²⁷ N. Grewe, *Z. Phys. B* **53**, 271 (1983).
 - ²⁸ H. Kojima, Y. Kuramoto, and M. Tachiki, *Z. Phys. B* **54**, 293 (1984).
 - ²⁹ F. B. Anders, *J. Phys.: Condens. Matter* **7**, 2801 (1995).
 - ³⁰ J. Kroha, P. Wölfle, and T. A. Costi, *Phys. Rev. Lett.* **79**, 261 (1997).
 - ³¹ K. Haule, S. Kirchner, J. Kroha, and P. Wölfle, *Phys. Rev. B* **64**, 155111 (2001).
 - ³² G. Baym and L. P. Kadanoff, *Phys. Rev.* **124**, 287 (1961).
 - ³³ G. Baym, *Phys. Rev.* **127**, 1391 (1962).
 - ³⁴ Y. Kuramoto and E. Müller-Hartmann, *J. Magn. Magn. Mater.* **52**, 122 (1985).
 - ³⁵ N. E. Bickers, *Rev. Mod. Phys.* **59**, 845 (1987).
 - ³⁶ R. Zitko and T. Pruschke, *Phys. Rev. B* **79**, 085106 (2009).
 - ³⁷ O. Sakai, Y. Shimizu, and T. Kasuya, *J. Phys. Soc. Jpn.* **58**, 3666 (1989).
 - ³⁸ R. Bulla, T. A. Costi, and D. Vollhardt, *Phys. Rev. B* **64**, 045103 (2001).
 - ³⁹ W. C. Oliveira and L. N. Oliveira, *Phys. Rev. B* **49**, 11986 (1994).
 - ⁴⁰ V. L. Campo and L. N. Oliveira, *Phys. Rev. B* **72**, 104432 (2005).
 - ⁴¹ M. Jarrell and J. E. Gubernatis, *Phys. Rep.* **269**, 133 (1996).
 - ⁴² C. Raas and G. S. Uhrig, *Eur. Phys. J. B* **45**, 293 (2005).
 - ⁴³ T. Saso, *Prog. Theor. Phys. Suppl.* **108**, 89 (1992).
 - ⁴⁴ Y. Kuramoto, *Z. Phys. B* **53**, 37 (1983).
 - ⁴⁵ J. Kroha and P. Wölfle, *J. Phys. Soc. Jpn.* **74**, 16 (2005).
 - ⁴⁶ Y. Kuramoto and H. Kojima, *Z. Phys. B* **57**, 95 (1984).
 - ⁴⁷ Y. Kuramoto, *Z. Phys. B* **65**, 29 (1986).
 - ⁴⁸ T. Brunner and D. C. Langreth, *Phys. Rev. B* **55**, 2578 (1997).
 - ⁴⁹ H. Keiter, *Z. Phys. B* **60**, 337 (1985).
 - ⁵⁰ H. Keiter and Q. Qin, *Z. Phys. B* **79**, 397 (1990).
 - ⁵¹ N. Kawakami and A. Okiji, *Phys. Lett. A* **9**, 483 (1981).
 - ⁵² N. Kawakami and A. Okiji, *Solid State Commun.* **43**, 467 (1983).
 - ⁵³ A. Okiji and N. Kawakami, *Solid State Commun.* **43**, 365 (1982).
 - ⁵⁴ B. Horvatic and V. Zlatic, *J. Phys.* **46**, 1459 (1985).
 - ⁵⁵ J. Otsuki, H. Kusunose, and Y. Kuramoto, *J. Phys. Soc. Jpn. Suppl.* **75**, 256 (2006).
 - ⁵⁶ A. Okiji and N. Kawakami, *Phys. Rev. Lett.* **50**, 1157 (1983).
 - ⁵⁷ B. Horvatic and V. Zlatic, *Solid State Commun.* **54**, 957 (1985).
 - ⁵⁸ P. Schlottmann, *Phys. Rev. Lett.* **50**, 1697 (1983).
 - ⁵⁹ H. Shiba, *Prog. Theor. Phys.* **54**, 967 (1975).
 - ⁶⁰ N. E. Bickers, D. L. Cox, and J. W. Wilkins, *Phys. Rev. B* **36**, 2036 (1987).
 - ⁶¹ M. Jarrell, J. E. Gubernatis, and R. N. Silver, *Phys. Rev. B* **44**, 5347 (1991).
 - ⁶² M. Jarrell, J. Gubernatis, R. N. Silver, and D. S. Sivia, *Phys. Rev. B* **43**, 1206 (1991).
 - ⁶³ E. Müller-Hartmann, *Z. Phys. B* **57**, 281 (1984).
 - ⁶⁴ H. O. Froyen, *Phys. Rev. B* **44**, 8433 (1991).
 - ⁶⁵ F. B. Anders, *Lecture Notes, Universität Bremen* (2004).
 - ⁶⁶ P. Coleman, *Phys. Rev. B* **29**, 3035 (1984).
 - ⁶⁷ The ionic transfer operators can be avoided by enlarging the Hilbert space and introducing auxiliary slave-bosons, which represent the empty state (see Coleman⁶⁶). The resulting standard Feynman perturbation-theory is in a one-to-one correspondence to the non-standard time-ordered Goldstone expansion described here.
 - ⁶⁸ Additionally, the numerics become unstable in these situations as it can be guessed from the strong fluctuations.